Supplementary information

Trans-switching in layered ferroelectrics

Pushpendra Gupta[1,†,*], Sergio Puebla[1,†], Fernando Gómez-Ortiz[2,†], Xinyan Li[3,†], Sajid Husain[1,*], Ting-Ran Liu[4], Peter Meisenheimer[5], Vishantak Srikrishna[5], Dmitri Nikonov[5], Matthew Chen[1], Yogesh Kumar[1], Ashish Omar[1], Barat Achinuq[6], Sujoy Roy[6], Yu-Tsun Shao[4], Yimo Han[3,7], Amrita Mathuriya[4], Sasikanth Manipatruni[4], Philippe Ghosez[2], Javier Junquera[8], and Ramamoorthy Ramesh[1,3,9*]

[1]*Department of Materials Science and Engineering, University of California, Berkeley, CA 94720, USA*
[2]*Theoretical Materials Physics, Q-Mat, Université de Liège, Sart-Tilman, B-4000, Belgium*
[3]*Rice Advanced Materials Institute, Rice University, Houston, TX 77005, USA.*
[4]*Mork Family Department of Chemical Engineering and Materials Science, University of Southern California, Los Angeles, CA 90089, USA.*
[5]*Kepler Computing, 617 River Oaks Pkwy, San Jose, CA, 95134, USA*
[6]*Advanced Light Source, Lawrence Berkeley National Laboratory, Berkeley, CA, 94720, USA*
[7]*Smalley-Curl Institute, Rice University, Houston, TX 77005, USA.*
[8]*Departmento de Ciencias de la Tierra y Física de la Materia Condensada, Universidad de Cantabria, Avenida de los Castros s/n, 39005, Santander, Spain*
[9]*Department of Physics, University of California, Berkeley, CA 94720, USA*

Contents

*E-mail: pushpendra@berkeley.edu, shusain@berkeley.edu, rramesh@berkeley.edu
† Authors contributed equally.

1 Theoretical analysis of distortion modes and trilinear couplings

In this section, we analyze the symmetry-allowed trilinear invariants involving the distortion modes present in the monoclinic Pc phase. As discussed in the main text, the high-symmetry $I4/mmm$ phase undergoes a symmetry lowering to the monoclinic Pc structure through the condensation of several lattice modes. A symmetry-adapted mode decomposition of the relaxed monoclinic polar phase identifies the following active distortion modes:

$$\Phi_x^+ \ (X_3^+),\ P_x \ (\Gamma_5^-),\ \Phi_z^- \ (X_1^-),\ \Phi_z^+ \ (X_2^+),\ P_z \ (\Gamma_3^-),\ \Phi_x^- \ (X_4^-),\ Q_x \ (\Gamma_5^+). \tag{1}$$

Clearly, all biquadratic couplings between the different modes are symmetry allowed. However, symmetry analysis reveals only seven allowed trilinear invariants, listed below in order of increasing importance, the amplitudes of the corresponding coefficients are given in Supplementary Table 1:

1. $P_x \times \Phi_x^+ \times \Phi_z^-$,
2. $P_z \times \Phi_x^+ \times \Phi_x^-$,
3. $P_z \times \Phi_z^+ \times \Phi_z^-$,
4. $P_x \times \Phi_z^+ \times \Phi_x^-$,
5. $P_x \times P_z \times Q_x$,
6. $Q_x \times \Phi_z^- \times \Phi_x^-$,
7. $Q_x \times \Phi_z^+ \times \Phi_x^+$.

Because the trilinear terms are highly interconnected, with individual modes appearing in multiple invariants, reversing any one participating mode inevitably triggers an avalanche of reversals among the others so that all trilinear couplings remain simultaneously satisfied. In the main text, we discussed the specific case in which the out-of-plane polarization is switched by an external electric field. This process is accompanied by the reversal of the Φ_x^- and Φ_z^- modes, which in turn induces the switching of P_x in order to satisfy all trilinear invariants in the free energy. However, as already anticipated in the main text, although there are compelling arguments suggesting that this pathway is the most likely, alternative switching scenarios also exist that simultaneously satisfy all trilinear invariants. In Supplementary Figure 1, we illustrate the symmetry-allowed switching pathways that respect all trilinear invariants upon reversing at least one polarization component. As one can see from Supplementary Figure 1, the first two switching pathways require the simultaneous reversal of both polarization components. In these cases, reversing either P_x or P_z inevitably forces the other to switch as well, since the involved rotations interlink them. These

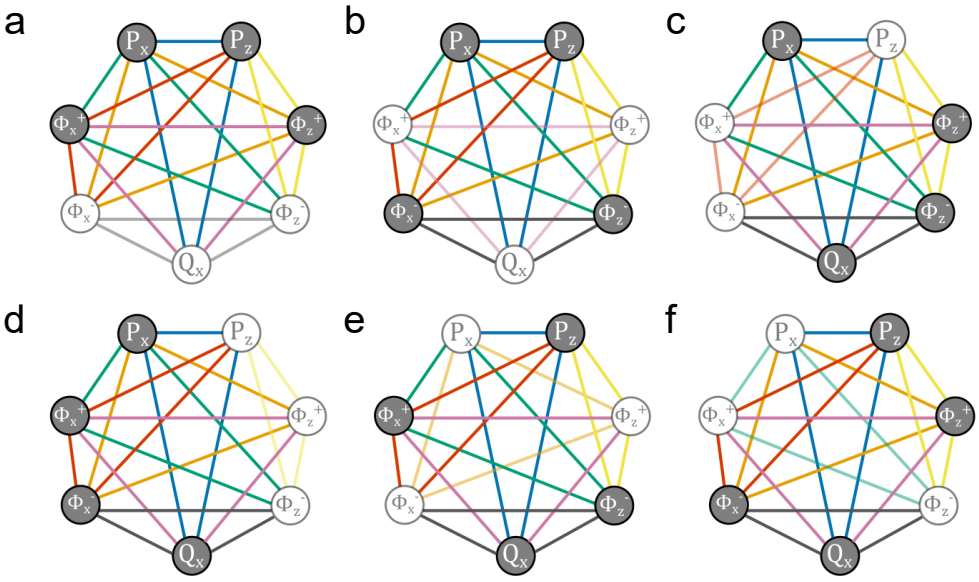

Supplementary Fig. 1. Network of symmetry allowed switching paths. Panels **a-f** show different consistent combinations of reverting modes switching one or more polarization components and respecting all trilinear couplings. Grey (white) circles indicate switching (preservation) of the associated mode.

pathways therefore correspond to fully cooperative switching mechanisms in which P_x, P_z, and the associated rotational modes invert together.

Alternatively, the remaining pathways illustrate that symmetry also permits the independent reversal of each polar mode—provided that the antipolar distortion Q_x and the corresponding rotational modes are reversed simultaneously. In these cases, the necessary trilinear invariants can still be satisfied without forcing both P_x and P_z to switch together. Thus, although a fully cooperative reversal of the two polarization components is possible, symmetry equally allows switching scenarios in which only one component flips. Determining which of these symmetry-allowed pathways is most likely to occur in practice requires evaluating their energy cost. It is important to note that the Γ_5^- as well as the antipolar Γ_5^+ and rotational modes $X_i^\pm$ are bidimensional ($2k$) in nature. A rigorous Landau treatment would therefore require two independent components for each of them. Although the two-dimensional character of the Γ_5^- mode is explicitly treated in order to reproduce its double-well structure, extending this fully two-dimensional description to all the modes as well as the trilinear and biquadratic couplings would be computationally prohibitive within DFT. Therefore, for simplicity, we treated the rotational and antipolar modes as one-dimensional distortions. The double-well structure of the in-plane polar (Γ_5^-) mode is, however, described within its full two-dimensional order-parameter space. In contrast, bilinear and trilinear couplings involving the in-plane polar mode are evaluated within an effective one-dimensional framework, by project-

ing the mode amplitudes onto its one-dimensional P_x subspace. The resulting model, including all biquadratic and trilinear coefficients, remains illustrative but does not capture the full multidimensional character of the modes and should thus be interpreted with caution (see Supplementary Table. 1 for the 1D coefficients of the model). The 2D double-well structure for the in-plane polar mode follows the following functional form,

$$-1275 \cdot (a^2 + b^2) + 705 \cdot (a^2 + b^2)^2 - 283.8 \cdot a^2 \cdot b^2$$

Alternatively, from an experimental standpoint, ptychography allows us to identify which of the symmetry-allowed switching paths are physically realized. The measurements as shown in Fig. 4 of the main text indicate that the switching is driven by the combined reversal of $P_x,\ P_z,\ \Phi_z^-,\ \Phi_x^-$, i.e. the switching path shown in Fig. 1b.

Table 1: Coefficients in meV per unit cell after normalization of the modes amplitude to 1 in the relaxed structure.

Coefficients	$\mathcal{E}$
$\alpha_{\Gamma_5^-}$	-1660
$\beta_{\Gamma_5^-}$	1046
$\alpha_{\Gamma_3^-}$	1.55
$\beta_{\Gamma_3^-}$	0.0
$\alpha_{X_1^-}$	-403
$\beta_{X_1^-}$	254
$\alpha_{X_2^+}$	-501
$\beta_{X_2^+}$	114
$\alpha_{X_3^+}$	-1810
$\beta_{X_3^+}$	1008
$\alpha_{X_4^-}$	0.08
$\beta_{X_4^-}$	0
$\alpha_{\Gamma_5^+}$	0.01
$\beta_{\Gamma_5^+}$	0
$\gamma_{\Gamma_5^-\Gamma_3^-}$	11
$\gamma_{\Gamma_5^-\Gamma_5^+}$	4
$\gamma_{\Gamma_3^-\Gamma_5^+}$	1
$\gamma_{\Gamma_5^- X_1^-}$	447
$\gamma_{\Gamma_5^- X_2^+}$	164
$\gamma_{\Gamma_5^- X_3^+}$	733
$\gamma_{\Gamma_5^- X_4^-}$	9
$\gamma_{\Gamma_3^- X_1^-}$	4
$\gamma_{\Gamma_3^- X_2^+}$	9
$\gamma_{\Gamma_3^- X_3^+}$	12
$\gamma_{\Gamma_3^- X_4^-}$	0
$\gamma_{\Gamma_5^+ X_1^-}$	1
$\gamma_{\Gamma_5^+ X_2^+}$	0
$\gamma_{\Gamma_5^+ X_3^+}$	1
$\gamma_{\Gamma_5^+ X_4^-}$	0
$\gamma_{X_1^- X_4^-}$	5
$\gamma_{X_2^+ X_3^+}$	213
$\gamma_{X_1^- X_2^+}$	102
$\gamma_{X_1^- X_3^+}$	365

Coefficients	$\mathcal{E}$
$\gamma_{X_2^+X_4^-}$	1
$\gamma_{X_3^+X_4^-}$	10
$\delta_{\Gamma_3^-\Gamma_5^-\Gamma_5^+}$	-15
$\delta_{\Gamma_5^-X_2^+X_4^-}$	-20
$\delta_{\Gamma_5^-X_3^+X_1^-}$	-1352
$\delta_{\Gamma_3^-X_2^+X_1^-}$	-24
$\delta_{\Gamma_3^-X_3^+X_4^-}$	-38
$\delta_{\Gamma_5^+X_1^-X_4^-}$	-8
$\delta_{\Gamma_5^+X_2^+X_3^+}$	-2

2 XLD-PEEM Studies

The asymmetry associated with the onset of ferroelectric order in thin films of this kind of materials leads to a difference at the Ti L_3 absorption edges between spectra measured with the x-ray linear polarization perpendicular and parallel to the ferroelectric polarization[1]. The angular dependence of the Ti t_{2g}/e_g intensity ratio follows the expected $\cos^2\alpha$ behavior characteristic of X-ray linear dichroism (see Supplementary figure 3), reflecting the projection of the electric-field vector onto anisotropic TiO_6 orbitals as shown previously in [2]. The differences in amplitude and phase between regions are commonly associated with distinct orbital anisotropies or ferroelectric domain orientations. Furthermore, we observe a shift in the positions of the t_{2g} and e_g spectra, and a difference in this behavior depending on the region of interest analyzed. In crystal-field theory, the splitting between t_{2g} and e_g orbitals is set by the parameter $10Dq$, which decreases or splits under octahedral distortion.[3–7] Although BTO is a low-symmetry layered oxide in which t_{2g} and e_g form bands rather than discrete levels, our data reveal a measurable angular modulation of the L_3 $e_g - t_{2g}$ separation. Supplementary Figure 4 shows a trend of closer centers in every ROI, with a steeper slope in ROIS 2 and 3, indicating a local distortion, enhanced Ti off-centering, or increased Ti–O hybridization, in agreement with the previous XLD results.

We also studied the O K-edge, shown in Supplementary Figure 5. Other studies reported the O K-edge energies are strongly material-dependent.[8] and that the O $1s \rightarrow 2p$–Ti $3d$ and O $2p$–Ti $4sp$ features shift by several eV due to variations in octahedral distortion or hybridization.[9,10] In Bi-containing Aurivillius phases, additional Bi–O hybrid states (Bi $6s/6p$–O $2p$) further modify and shift the higher-energy region of the O K edge.[11] Notably, we observe systematic energy shifts when rotating the X-ray polarization from parallel to perpendicular to the surface. This angular dependence can arise from anisotropic O $2p$ hybridization with Ti $3d/4sp$ and Bi $6p$ states in the distorted lattice, such difference in polarizations probe distinct subsets of unoccupied states. Similar polarization-dependent shifts have been reported in angle-resolved soft X-ray studies of anisotropic oxides.[12]

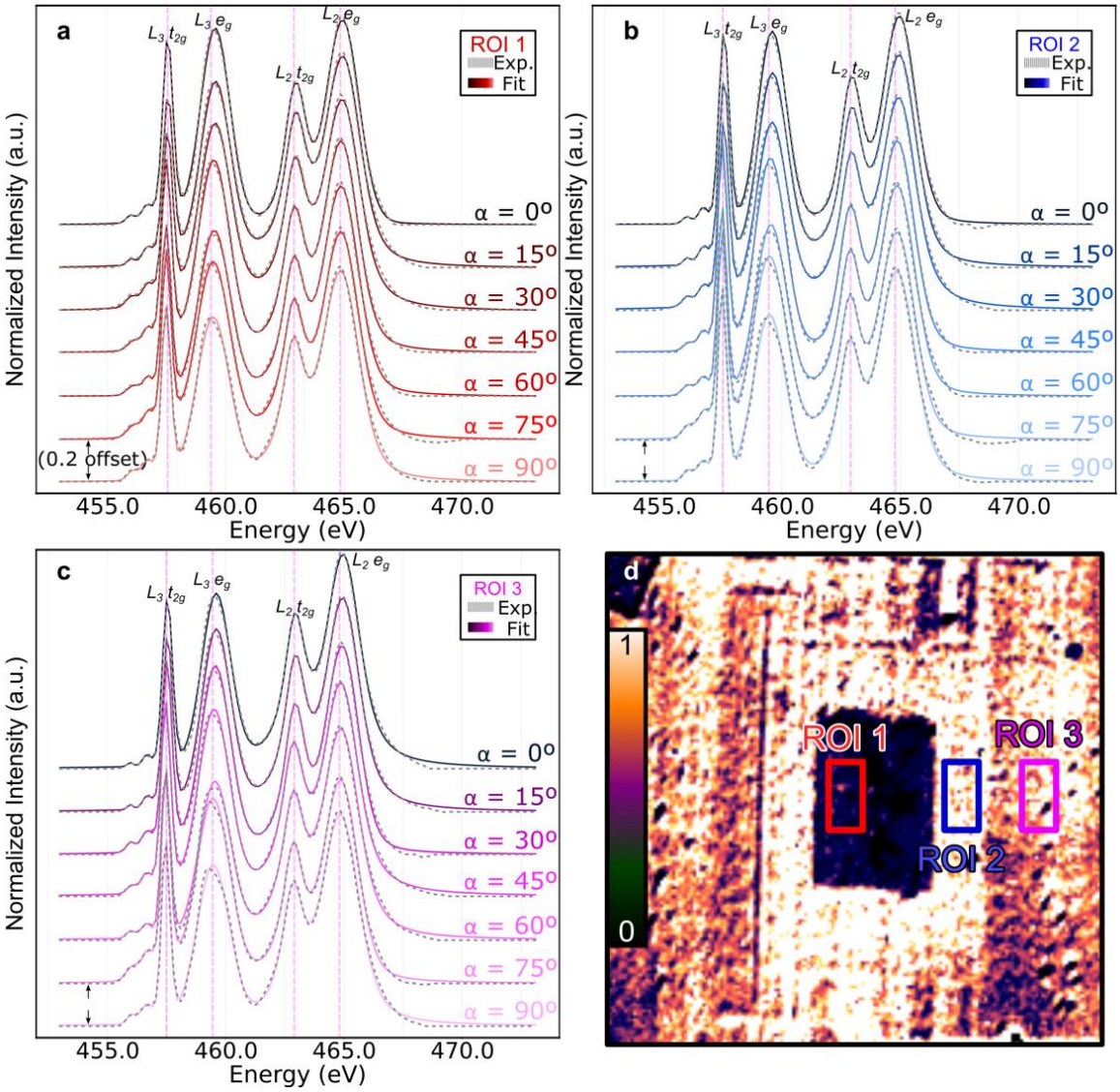

Supplementary Fig. 2. Incident-angle dependence of the Ti L-edge XAS for different regions of the BTO film. Light-incident-angle dependence of the Ti L-edge XAS for (a) ROI 1 (experimental data in dashed gray and fit in red tones), (b) ROI 2 (experimental data in dashed gray and fit in blue tones), and (c) ROI 3 (experimental data in dashed gray and fit in purple tones). Every data has been normalized to the L_3 e_g peak and an offset of 0.2 has been added to show clearly its angle dependence. Purple dashed vertical lines have been added as a guide for the eye to note the energy shift of every peak. (d) shows the contrast XLD PEEM image of the polarized region, showing ROI 1 and ROI 2 correspond to regions polarized by AFM with $+15$ V and -15 V, respectively, whereas ROI 3 represents an unpoled (virgin) area of the BTO film. A more pronounced angular shift of the t_{2g} and e_g features is observed in ROI 1 and ROI 2 compared with ROI 3, consistent with enhanced anisotropy in the ferroelectrically poled regions.

Table 2: Ti $L_{2,3}$ fitted peak parameters for ROI 1 as a function of polarization angle α. Values are reported as Center (eV) / FWHM (eV) / Maximum Normalized Experimental value.

α (deg)	$L_3\, t_{2g}$	$L_3\, e_g$	$L_2\, t_{2g}$	$L_2\, e_g$
0	457.56 / 0.52 / 0.88	459.56 / 1.46 / 0.94	462.96 / 1.09 / 0.68	464.95 / 1.62 / 1.00
15	457.56 / 0.52 / 0.78	459.57 / 1.53 / 0.86	462.96 / 1.17 / 0.72	464.97 / 1.72 / 1.00
30	457.55 / 0.51 / 0.83	459.56 / 1.60 / 0.86	462.93 / 1.18 / 0.71	464.95 / 1.72 / 1.00
45	457.50 / 0.51 / 0.89	459.50 / 1.56 / 0.88	462.90 / 1.14 / 0.68	464.89 / 1.67 / 1.00
60	457.49 / 0.48 / 0.79	459.52 / 1.55 / 0.75	462.89 / 1.14 / 0.66	464.89 / 1.71 / 1.00
75	457.49 / 0.48 / 0.89	459.47 / 1.65 / 0.83	462.87 / 1.16 / 0.67	464.89 / 1.73 / 1.00
90	457.49 / 0.47 / 0.81	459.46 / 1.63 / 0.76	462.86 / 1.18 / 0.68	464.88 / 1.80 / 1.00

Table 3: Ti $L_{2,3}$ fitted peak parameters for ROI 2 as a function of polarization angle α. Values are reported as Center (eV) / FWHM (eV) /Maximum Normalized Experimental value

α (deg)	$L_3\, t_{2g}$	$L_3\, e_g$	$L_2\, t_{2g}$	$L_2\, e_g$
0	457.55 / 0.52 / 0.90	459.59 / 1.42 / 0.89	462.95 / 1.08 / 0.70	464.97 / 1.63 / 1.00
15	457.55 / 0.51 / 0.86	459.60 / 1.50 / 0.89	462.95 / 1.14 / 0.74	464.97 / 1.67 / 1.00
30	457.53 / 0.50 / 0.87	459.58 / 1.56 / 0.85	462.92 / 1.16 / 0.73	464.95 / 1.71 / 1.00
45	457.49 / 0.49 / 0.96	459.51 / 1.50 / 0.87	462.88 / 1.10 / 0.69	464.88 / 1.68 / 1.00
60	457.47 / 0.45 / 0.86	459.53 / 1.52 / 0.77	462.87 / 1.12 / 0.69	464.89 / 1.72 / 1.00
75	457.48 / 0.46 / 0.98	459.47 / 1.63 / 0.86	462.86 / 1.13 / 0.69	464.88 / 1.74 / 1.00
90	457.48 / 0.44 / 0.89	459.47 / 1.59 / 0.76	462.85 / 1.13 / 0.68	464.87 / 1.82 / 1.00

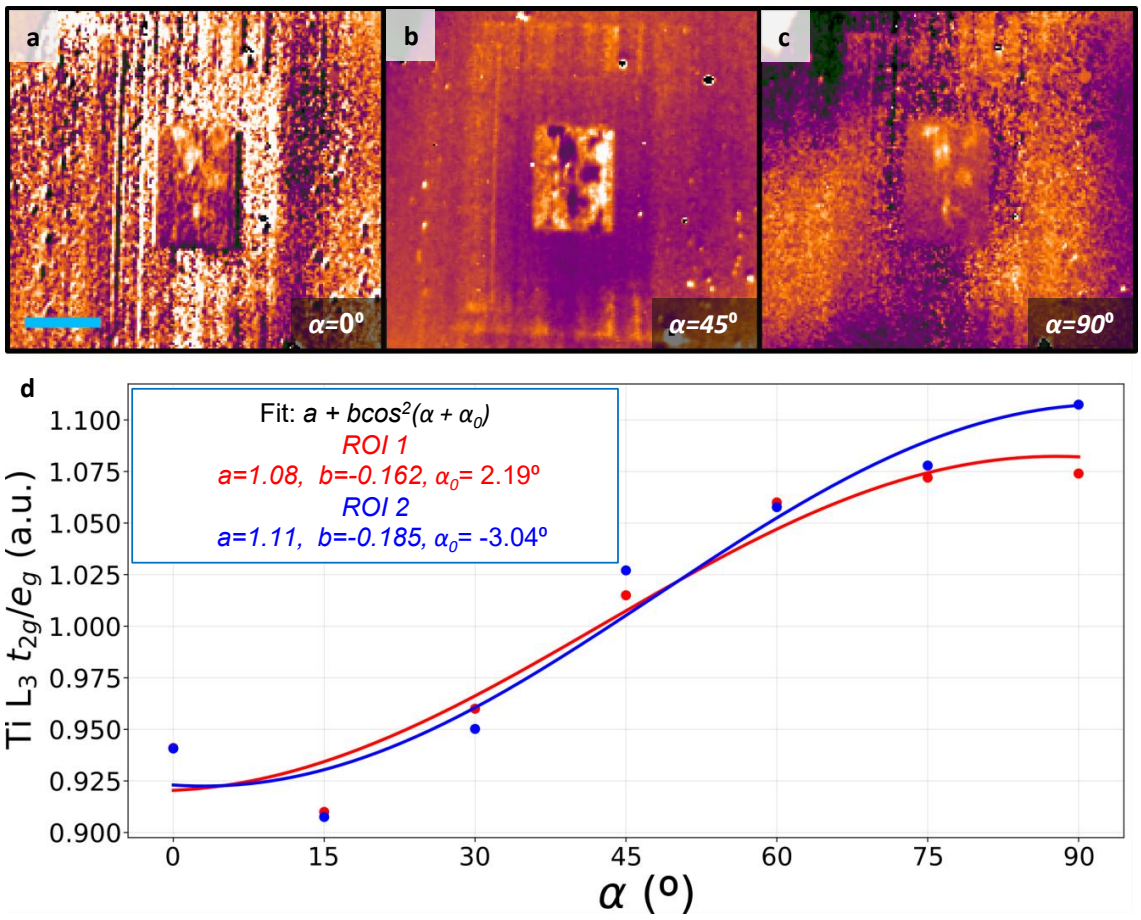

Supplementary Fig. 3. Angle dependence of Ti L_3 t_{2g}/e_g orbitals. (a-c) PEEM images belonging to division of maximum of t_{2g}/e_g peaks with a incident polarization angle of 0º, 45º and 90º, respectively. These images show an angle dependence between both ROIs. Color scale bar in (a) is 5 μm (d) Angle dependence of the light polarization used from α =0º parallel to α =90º perpendicular to the sample surface, proving the in-plane orientation of the ferroelectric domains in ROI 1 and 2.

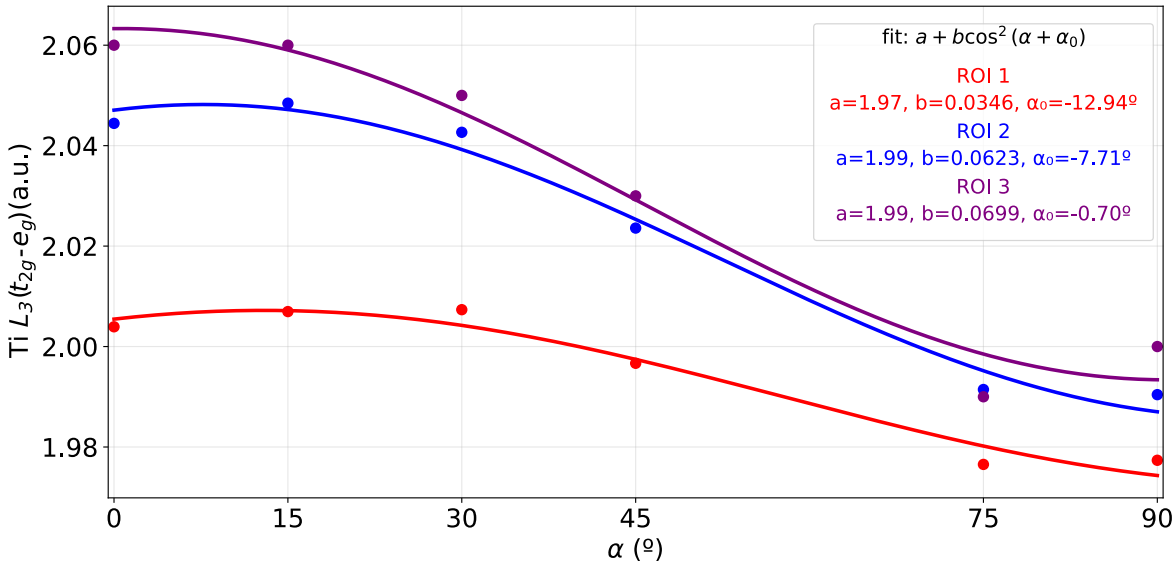

Supplementary Fig. 4. Ti L_3 Difference between center of Ti L_3 t_{2g} and e_g orbitals. Difference between the the centers of Ti L_3 t_{2g} and e_g orbitals in the regions of interest 1 (blue), 2 (red) and 3 (purple), suggesting a possible distortion of the TiO_6 octahedra.

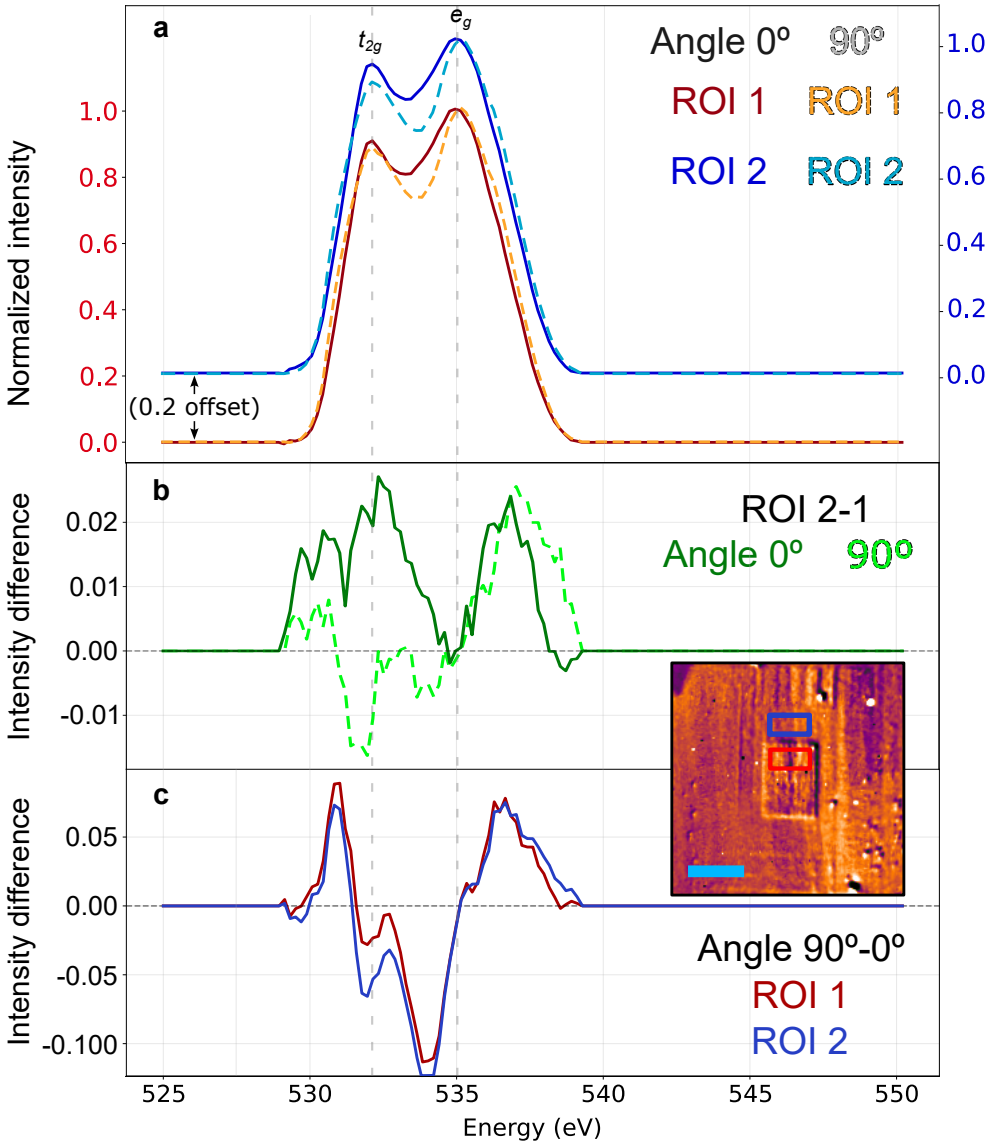

Supplementary Fig. 5. XLD PEEM of O K-edge in a polarized area. (a) Normalized intensity with background subtracted of the O K-edge, noting the t_{2g} and e_g orbitals. Solid dark tones lines belong to angle 0º of polarization, (parallel to the sample), and dashed light color lines correspond to 90º (perpendicular to the sample surface). ROI 1 and 2 are colored in red and blue tones, respectively. An artificial offset of 0.2 has been added between the ROI 1 and 2 for clarity. Dashed vertical gray lines serve as guides for the eye, placed at the maximum of the peaks. (b) Intensity difference between the ROI 1 and 2 with a polarization angle of 0º, parallel to the sample surface, with dark solid green line; and 90º, perpendicular to the sample surface, with a dashed light green line. (c) XLD, intensity difference between the perpendicular and parallel incidence light, of the ROI 1 and 2 in solid red and blue lines, respectively. Inset: XLD contrast of PEEM image at the maximum of the O K-edge t_{2g} orbital, the two rectangles in red and blue belong to the ROI 1 and 2, respectively. Light-blue scale bar is 5 μm.

3 HAADF STEM studies

High-angle annular dark-field scanning transmission electron microscopy (HAADF-STEM) further corroborates the epitaxial alignment between the [010]/[001] zone axes of the BTO film and the [110] zone axis of $SrRuO_3$/$SrTiO_3$ (Supplementary Fig. 4). High density of 90° ferroelastic domains is observed within the as-grown BTO film, attributed to the cubic symmetry of the $SrTiO_3$ substrate (Supplementary Fig. 5). Despite the presence of localized stacking faults (Supplementary Fig. 6), the high crystallinity of the pristine BTO film is demonstrated by the atomic-resolution images. Collectively, the comprehensive structural analyses by AFM, XRD, and STEM unequivocally demonstrate that the synthesized BTO thin films possess outstanding crystalline quality, smooth morphology, and precise epitaxial order. These results establish a robust foundation for advanced investigations of their functional and ferroelectric properties.

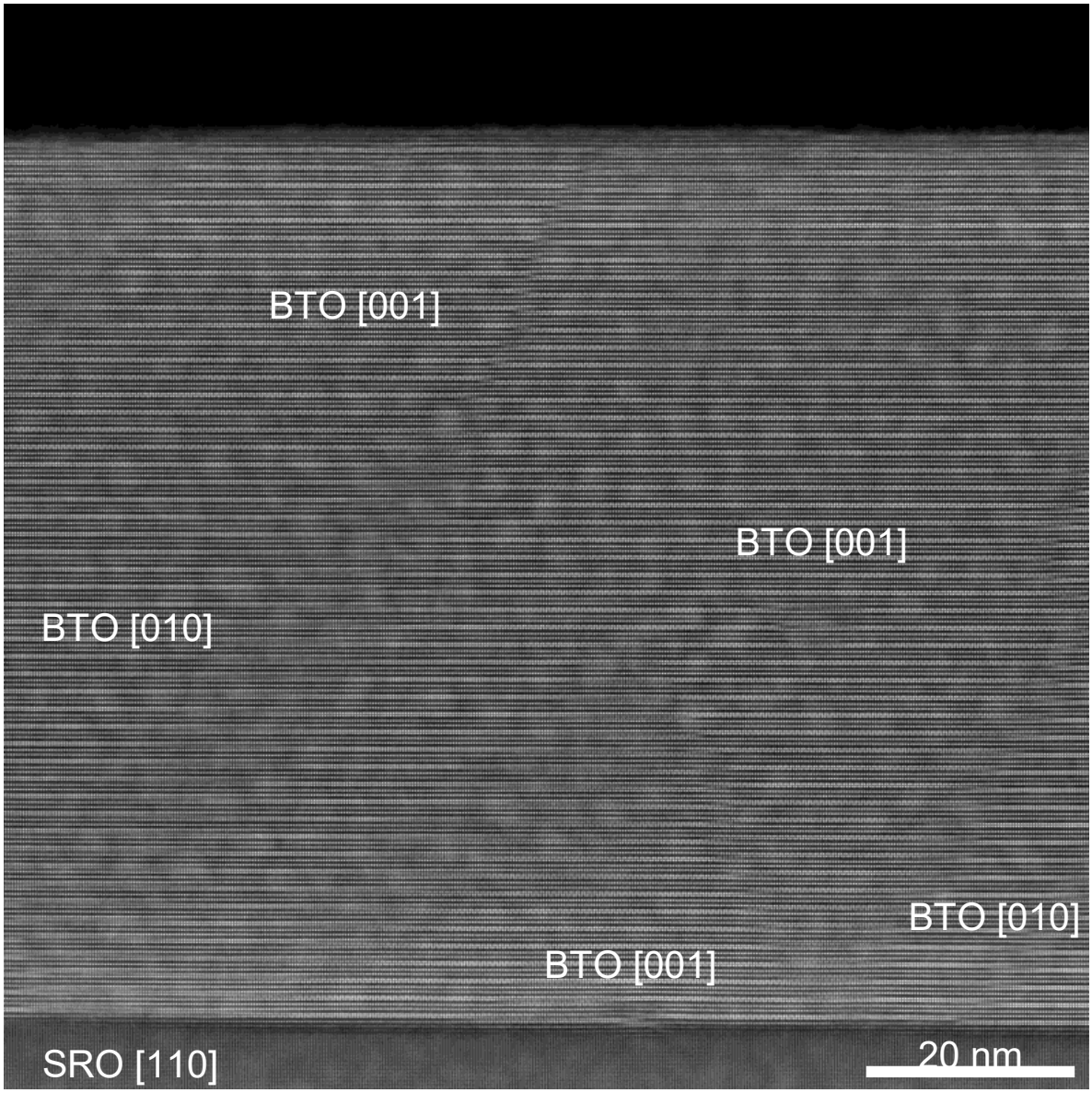

Supplementary Fig. 6. A low magnification STEM image showing the epitaxial alignment of BTO [010]/[001] zone axes with SRO [110] zone axis.

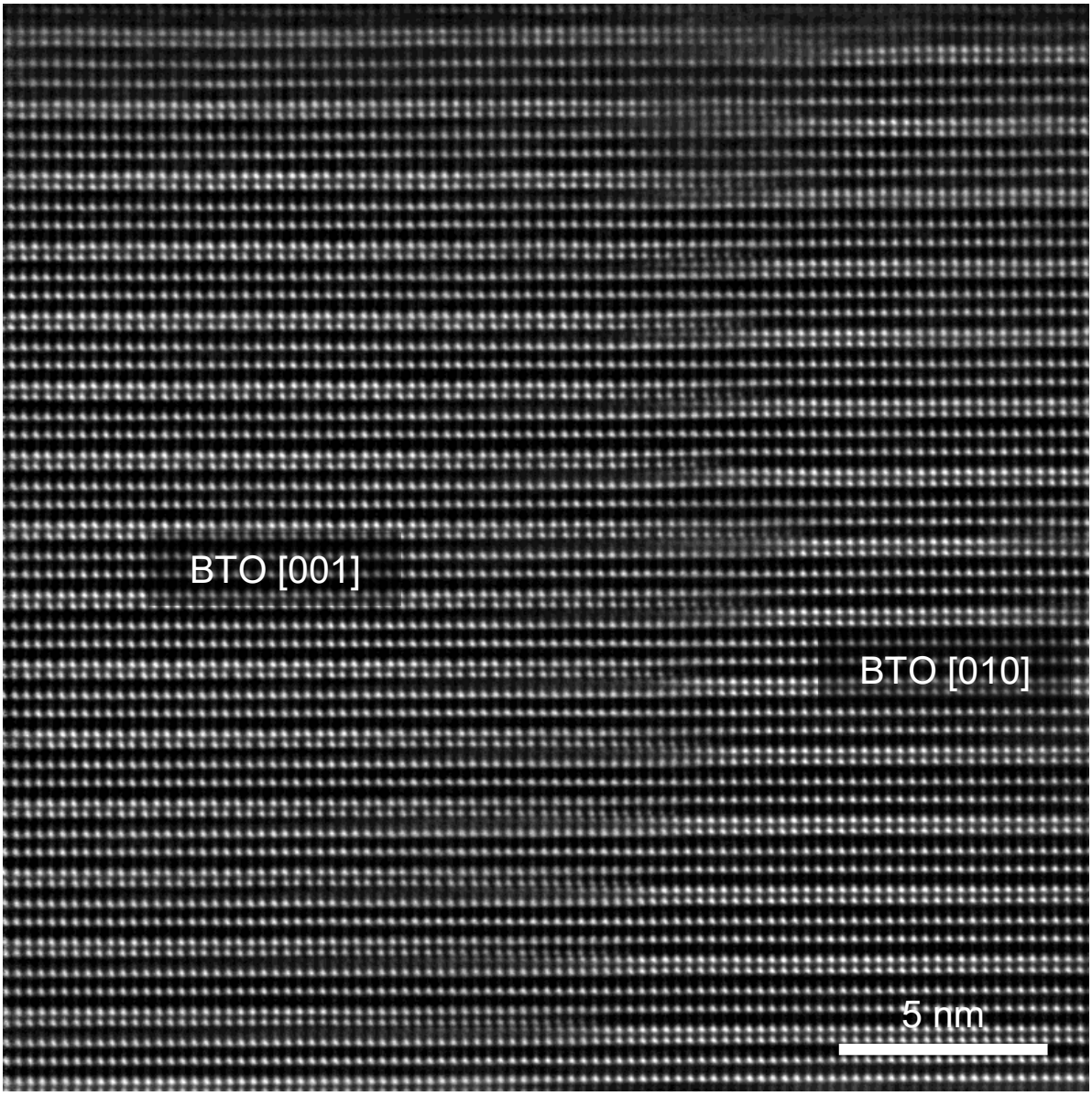

Supplementary Fig. 7. A high magnification HAADF-STEM image showing the formation of a 90° ferroelastic domain wall between BTO [001] and [010] domains.

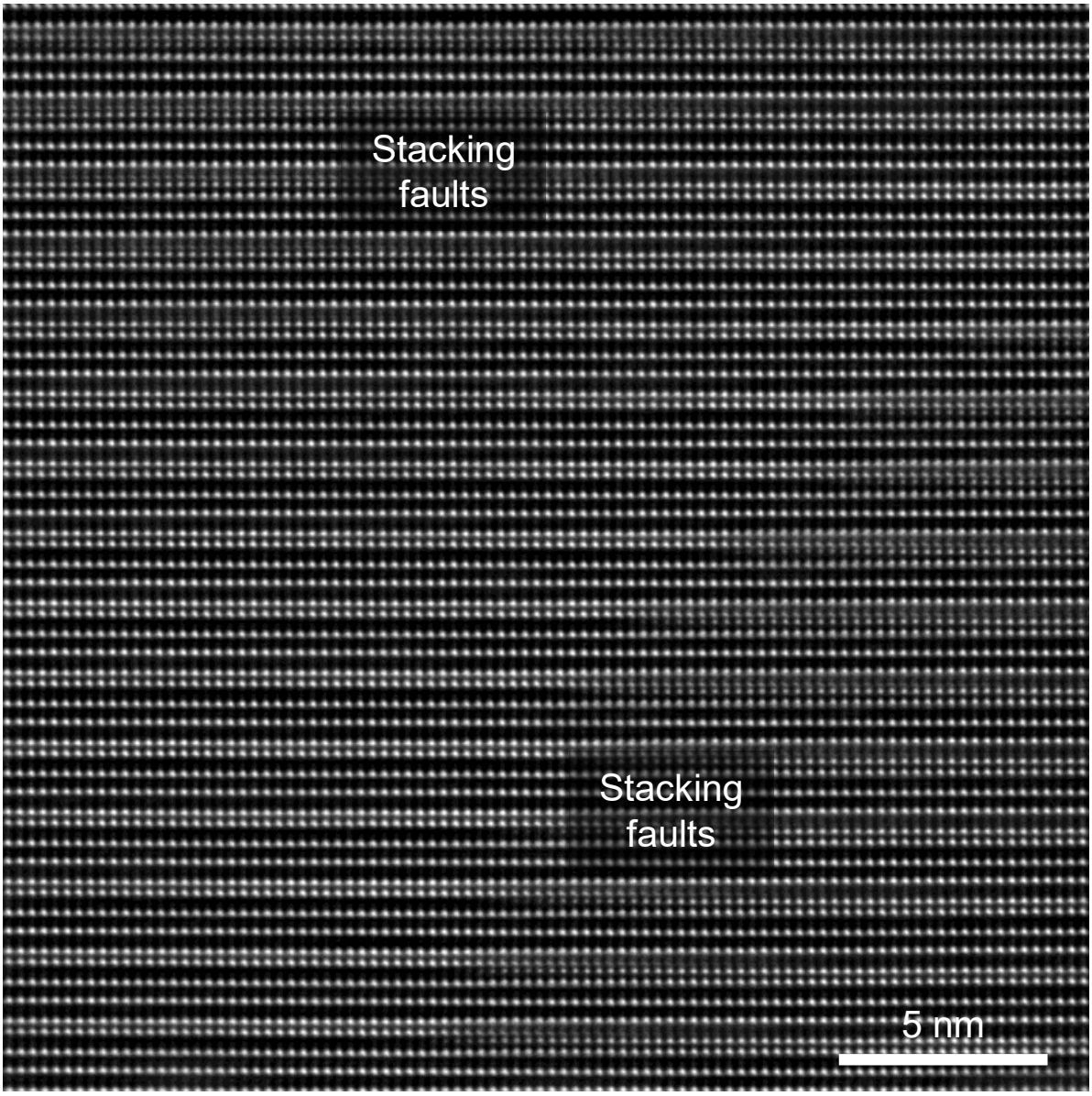

Supplementary Fig. 8. Lattice coherent stacking faults within BTO [010] domain, which is likely originated from atomic stages on the substrate surface.

References

1. Arenholz, E. *et al.* Probing ferroelectricity in pbzr 0.2 ti 0.8 o 3 with polarized soft x rays. *Physical Review B—Condensed Matter and Materials Physics* **82**, 140103 (2010).

2. Polisetty, S. *et al.* X-ray linear dichroism dependence on ferroelectric polarization. *Journal of physics: Condensed matter* **24**, 245902 (2012).

3. Abbate, M. *et al.* Soft-x-ray-absorption studies of the location of extra charges induced by substitution in controlled-valence materials. *Physical Review B* **44**, 5419 (1991).

4. Higuchi, T. *et al.* Electronic structure in valence band of nd-substituted $\mathrm{Bi_4Ti_3O_{12}}$ single crystal probed by soft-x-ray emission spectroscopy. *Japanese journal of applied physics* **44**, L1491 (2005).

5. Song, Y. *et al.* Unconventional crystal-field splitting in noncentrosymmetric $\mathrm{BaTiO_3}$ thin films. *Physical review materials* **4**, 024413 (2020).

6. Subías, G., García, J., Sánchez, M., Blasco, J. & Proietti, M. Soft x-ray absorption spectroscopy $(\mathrm{MnL_{2,3}and O_K})$ in mixed valence manganites. *Surface Review and Letters* **9**, 1071–1078 (2002).

7. Zhang, J. *et al.* High-resolution electron energy-loss spectroscopy of $\mathrm{BaTiO_3}$/ $\mathrm{SrTiO_3}$ multilayers. *Physical Review B—Condensed Matter and Materials Physics* **71**, 064108 (2005).

8. Kim, Y. *et al.* Enhancement of photo-oxidation activities depending on structural distortion of fe-doped $\mathrm{TiO_2}$ nanoparticles. *Nanoscale Research Letters* **11**, 41 (2016).

9. De Groot, F. *et al.* Oxygen 1s x-ray-absorption edges of transition-metal oxides. *Physical Review B* **40**, 5715 (1989).

10. Wu, Z., Ouvrard, G., Gressier, P. & Natoli, C. Ti and ok edges for titanium oxides by multiple scattering calculations: Comparison to XAS and EELS spectra. *Physical Review B* **55**, 10382 (1997).

11. Jovic, V. *et al.* Soft x-ray spectroscopic studies of the electronic structure of $\mathrm{M : BiVO4(M = Mo, W)}$ single crystals. *Journal of Materials Chemistry A* **3**, 23743–23753 (2015).

12. Huang, W. *et al.* Enhanced orbital anisotropy through the proximity to a $\mathrm{SrTiO_3}$ layer in the perovskite iridate superlattices. *Physical Review B* **104**, 075156 (2021).